

Article

Electronic Structure of Rh and Ir Single Atom Catalysts Supported on Defective and Doped ZnO: Assessment of Their Activity Towards CO Oxidation

Arda Erbasan ¹, Hande Ustunel ^{1,*} and Daniele Toffoli ^{2,3,*}

¹ Department of Physics, Middle East Technical University, Dumlupinar Blv 1, Ankara 06800, Turkey; arda.erbasan@metu.edu.tr

² Dipartimento di Scienze Chimiche e Farmaceutiche, Università degli Studi di Trieste, Via L. Giorgieri 1, 34127 Trieste, Italy

³ IOM-CNR, Istituto Officina dei Materiali-CNR, S.S.14, Km 163.5, 34149 Trieste, Italy

* Correspondence: ustunel@metu.edu.tr (H.U.); toffoli@units.it (D.T.)

Abstract: This study investigated the electronic structure of single-atom Rhodium (Rh) and Iridium (Ir) adsorbed on defective and impurity-doped ZnO(0001) surfaces, and assessed their activity towards the CO oxidation reaction. Our findings reveal that surface impurities significantly influence the binding energies and electronic properties of the metal atoms, with Al and Cr serving as particularly effective promoters. While Rh and Ir acquire a positive charge upon incorporation on the unpromoted Zn(0001) surface, adsorption directly on the promoter results in a net negative charge, thus facilitating the activation of both CO and O₂ species. These results highlight the potential of impurity-promoted ZnO surfaces in modulating and tailoring the electronic properties of SACs, which can be used for a rational design of active single-atom catalysts.

Keywords: density functional theory; single atom catalysis; CO activation; O₂ activation; oxidation reaction



Citation: Erbasan, A.; Ustunel, H.; Toffoli, D. Electronic Structure of Rh and Ir Single Atom Catalysts Supported on Defective and Doped ZnO: Assessment of Their Activity Towards CO Oxidation. *Molecules* **2024**, *29*, 5082. <https://doi.org/10.3390/molecules29215082>

Academic Editor: M. Natália D.S. Cordeiro

Received: 14 September 2024

Revised: 20 October 2024

Accepted: 25 October 2024

Published: 28 October 2024



Copyright: © 2024 by the authors. Licensee MDPI, Basel, Switzerland. This article is an open access article distributed under the terms and conditions of the Creative Commons Attribution (CC BY) license (<https://creativecommons.org/licenses/by/4.0/>).

1. Introduction

Single-atom catalysts (SACs) represent the upper limit of surface-to-volume ratio achievable by the metal component of a heterogeneous catalyst while offering higher resistance against erosion and poisoning than their larger counterparts [1]. SACs, on the other hand, are susceptible to facile diffusion and loss of reactivity via segregation [2]. In general [3–5], a complex relation between the metal atoms and the support determines the stability, activity, and selectivity of the metal atom for a given reaction [6–9].

Transition metal atoms dispersed on oxide supports are a prevalent category of SACs [10]. Oxide supports are frequently employed due to their cost-effectiveness, stability, and the abundance of active sites on their surfaces. In addition, oxide supports feature various defects, such as oxygen and metal vacancies, edges, steps, and terraces, which serve as anchor sites for single metals [11,12]. This characteristic has been utilized in various catalyst designs. For instance, Zhou et al. [13] showed that the surface arrangement of Pt single atoms could be controlled by modifying the coordination environment on TiO₂ supports using defect engineering techniques. Similarly, stabilizing single-atom sites via oxygen vacancies was shown to increase the performance of a Rh-SnO₂ catalyst towards the gas-phase hydroformylation of ethylene [14]. Beyond oxygen vacancies, cation vacancies also function as effective anchor sites. As an example, stabilizing single metals by lattice oxygens in a metal vacancy site has been demonstrated to increase the efficacy of Pt-CrO₂ [15] and Pt/Au-ZnO [16] towards wet CO oxidation and methanol steam reforming, respectively. Furthermore, metal oxides can readily exchange electrons with metals, potentially improving their reactivity and selectivity by causing a shift of their *d* orbitals [17]. Shi et al. [18] reported that *d* orbital occupation of a Au atom placed on

oxygen-deficient TiO₂ can be controlled through substrate doping, thereby enhancing its catalytic efficiency.

In addition to employing vacancy-type defects, the performance of SACs can be further tuned by introducing a second metal as a promoter. For instance, Searles et al. demonstrated that silica-supported Ga-Pt nanoparticles generated from single-atom sites are highly effective and stable towards propane dehydrogenation [19]. Other notable examples include silica-supported Pt-Zn [20] and silica-supported Pt-Ti [21], which are also used for propane dehydrogenation.

This study investigates single Rh and Ir atoms supported on defective and metal-decorated ZnO(0001) surfaces for CO oxidation. Specifically, it examines how surface impurities, acting as promoters, influence their electronic properties and, as a consequence, their catalytic properties. ZnO has attracted significant attention in the last few years as a support for SACs thanks to its stability, optical properties, and nontoxicity [22–25]. In the context of SACs, the ability to stabilize metal atoms through the creation of surface defects has been shown to yield highly efficient catalysts. For instance, a theoretical study by Jacobo-Fernandez et al. proposed magnetic SACs with Pt and Pd on defective ZnO surfaces as an efficient catalyst for the oxygen reduction reaction [25]. Mohite et al. designed and measured the performance as photocatalysts of single Au atoms on defective ZnO surfaces [26]. In a different geometric configuration, ZnO quantum dots with transition metal single atoms (Fe, Co, Ni, Cu) have been used as catalysts for the conversion of glycerol to glycerol carbonate [23].

Our choice of Rh and Ir as the metal atoms is largely motivated by the fact that there have not been many studies combining their well-known catalytic properties and the advantages of ZnO as a support. Rh, in particular, has been extensively investigated with other supports including Al₂O₃ [27,28], CeO₂ [29,30], phosphotungstic acid [31–33], graphdiyne [34], TiO₂ [35,36], FeO_x [37], and ZnO nanowires (nw) [22]. Notably, Han et al. [22] demonstrated that Rh supported on ZnO-nw exhibits very high catalytic activity toward dry CO oxidation reaction compared to Au and Pt single metals. Rh has also been investigated for reactions such as hydroformylation [38–41], formic acid electro-oxidation [42], and CO₂ reduction [43]. Lang et al. further confirmed that Rh SAC supported by ZnO-nw shows excellent catalytic activity and stability for the hydroformylation of olefins [41].

In contrast, there are fewer studies on Ir as a single metal [44–49]. However, there are some examples where Rh and Ir were investigated together for CO oxidation on hexagonal boron nitride nanosheets [50], zeolites [51], GeS monolayer [52], MgO and Al₂O₃ [53,54], and polyoxometalate [55]. A few examples in which Rh and Ir were dispersed on a ZnO support can be found [7,56,57].

The CO oxidation reaction is widely recognized as a benchmark for evaluating catalytic activity [58,59]. To facilitate the investigation of reactivity, several descriptors have been employed, including the adsorption energies of reactants and products [60,61], partial density of states (PDOS) profiles and *d*-band centers [62], partial charges and charge transfer [63], and molecular bond lengths and stretching mode frequencies [64]. In this study, we applied these descriptors to assess the catalytic potential of Rh and Ir single atoms toward CO oxidation on defective and promoted ZnO(0001) surfaces. In selecting the promoters, a diverse range was considered: Al represented low-valent metals, Cr was a magnetic impurity, Pd was included as a noble metal, and Cu was chosen for its well-known reactivity.

The plan of the paper is as follows: In Section 2, we present the computational details. Section 3 collects our results along with their interpretation and analysis. Section 4 summarizes the outcomes of this work.

2. Computational Details

All calculations were performed within the density functional theory (DFT) framework as implemented in the Vienna Ab Initio Simulation Package (VASP) [65–67]. Electronic exchange and correlation was described using the Perdew–Burke–Ernzerhof (PBE) formal-

ism [68] while electron–ion interactions were described by the projector-augmented-wave (PAW) scheme [69,70]. 3d-4s, 2s-2p, 2s-2p, 4d-5s, 5d-6s, 3s-3p, 3d-4s, 3d-4s, and 4d-5s electrons of Zn, O, C, Rh, Ir, Al, Cr, Cu, and Pd were included in the calculations as valence electrons, respectively. Geometry optimization was carried out until all forces reached 0.01 eV/Å with an electron energy convergence of 10^{-5} eV. All calculations were performed with spin polarization. The plane-wave basis was truncated using a kinetic energy cutoff of 600 eV. A Hubbard correction was employed with $U_{eff} = 5$ eV for the on-site Coulomb interaction on Zn-*d* orbitals as described by Dudarev et al. [71]. This choice for the U_{eff} was motivated by its ability to give lattice constants in closer agreement with experimentally determined lattice constants compared to other theoretical studies using different U_{eff} values for ZnO [72].

The Zn-terminated ZnO(0001) surface was modeled using six-layer slabs with 2×2 and 3×3 periodically repeating surface units to test for coverage effects. Γ -centered Monkhorst-Pack grids of $11 \times 11 \times 1$ and $7 \times 7 \times 1$ were employed for Brillouin zone integrations for the 2×2 and 3×3 cells, respectively. A minimum vacuum spacing of 14.5 Å was employed for all calculations to reduce interactions between adjacent periodic images. Geometric optimization of the surfaces resulted in the inward relaxation of top layers, as also noted in the literature [73].

Some descriptors used in this work to assess reactivity were adsorption energies, charge density differences upon adsorption, bond lengths, bond stretching mode frequencies, partial charges, and partial density of states (PDOS) profiles. Adsorption energies were calculated using

$$E_b = E_{tot} - E_{surf} - E_{ads} \quad (1)$$

where E_{tot} , E_{surf} , and E_{ads} are the electronic ground state energies of the system, the surface, and the isolated adsorbate, respectively. With this definition, negative energies indicate stable adsorption. Charge density difference (CDD) contours were calculated in a similar way via the expression

$$\Delta\rho(\vec{r}) = \rho_{tot}(\vec{r}) - \rho_{surf}(\vec{r}) - \rho_{ads}(\vec{r}) \quad (2)$$

where $\rho_{tot}(\vec{r})$, $\rho_{surf}(\vec{r})$, and $\rho_{ads}(\vec{r})$ are the electronic ground state density of the system, the surface, and the isolated adsorbate, respectively. Vibrational frequencies were calculated by diagonalizing the force constant matrix obtained by central finite differences with a step size of 0.01 Å. During the calculation of the frequencies, the adsorbing species as well as the metals were allowed to move. Finally, Bader decomposition was used to calculate partial charges using the software developed by the Henkelman (version 1.05) group [74].

3. Results and Discussion

3.1. Substitutional Incorporation of Rh and Ir Atoms on the ZnO(0001) Surface

In this study, we considered two methods of introducing the single-atom component to the support surface: substitutional and adsorbed. Starting with a perfect surface, we first substituted a Rh or Ir atom in place of a Zn atom on the 2×2 surface. Beyond stabilizing the single atom, the new coordination environment arising from substitutional incorporation of a metal atom would also modify its charge state and the position of its *d* orbitals, possibly altering its reactivity. Upon geometry relaxation, both the Rh and the Ir atoms were seen to undergo a noticeable elevation with respect to the original position of Zn, as illustrated in Figure 1.

This elevation was even more pronounced in the case of Rh. A Bader charge decomposition analysis, also shown in the Figure 1, reveals that upon adsorption, Rh and Ir attained partial charges of +0.43 $|e|$ and +0.34 $|e|$, respectively.

Next, we investigated the adsorption characteristics of the relevant species involved in the CO oxidation reaction, namely CO, O₂, and O. In actual experimental settings, there may be a wide variety of SAC coverages. For instance, Xue et al. [75] investigated Pt loadings on CdS nanosheets ranging from 0.3% to 3% weight. HAADF-STEM images

of their loading clearly show several instances of metal atoms that are no further than a few lattice sites. Since lateral interactions between adsorbates can significantly influence adsorption behavior [76], we first assessed the importance of coverage, in preparation for the rest of our results. To this end, we considered adsorption in both a 2×2 (1/4 coverage) and a 3×3 (1/9 coverage) periodic surface cell. The optimized CO, O₂, and O adsorption geometries, energies, and partial charges are reported in Figure 2 and Table 1 for these coverages.

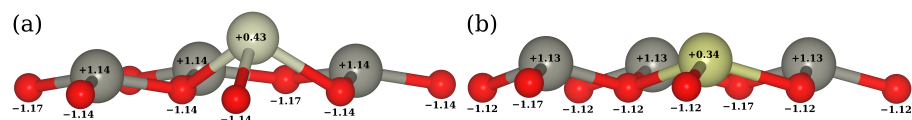


Figure 1. Optimized geometry and Bader charges on the Rh (a) and Ir (b) atoms in substitutional positions on the ZnO(0001) surface. The charges on the nearest O and Zn atoms are also shown. In this figure, light gray, red, dark gray, and yellow spheres represent Rh, O, Zn, and Ir atoms, respectively.

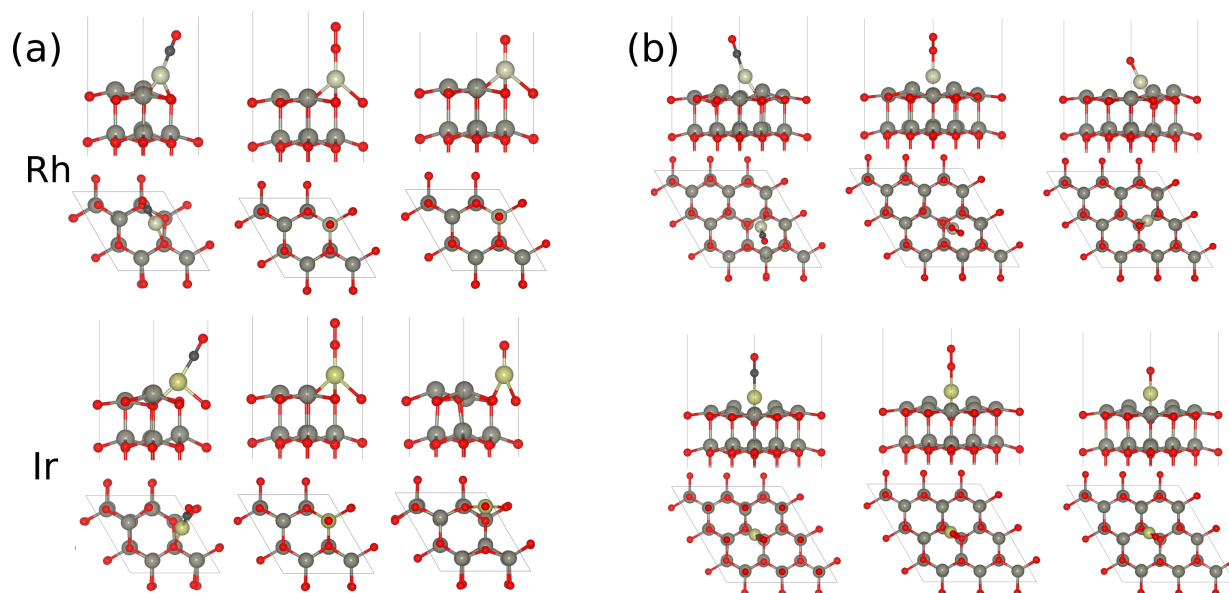


Figure 2. Optimized CO, O₂, and O adsorption geometries on the 2×2 (a) and 3×3 (b) ZnO(0001) surfaces. In this figure, light gray, red, black, dark gray, and yellow spheres represent Rh, O, C, Zn, and Ir atoms, respectively.

Table 1. Adsorption energies (E_b), Bader charges (q), vibrational frequencies (f), and bond distances (d) of CO, O₂, and O adsorption on 2×2 and 3×3 Rh- and Ir-decorated ZnO(0001). The subscript X represents either Rh or Ir, while A and B correspond to the individual atoms of the adsorbate, respectively. A^* designates the atom directly in contact with the surface (e.g., in the case of CO, A^* is C.) The stretch mode frequencies reported for O correspond to the O- X bond.

	CO				O ₂				O			
	2×2		3×3		2×2		3×3		2×2		3×3	
	Rh	Ir	Rh	Ir	Rh	Ir	Rh	Ir	Rh	Ir	Rh	Ir
E_b [eV]	-2.74	-3.85	-3.43	-3.97	-1.47	-1.97	-2.01	-2.07	-4.77	-6.68	-5.80	-6.40
q_X [e]	0.44	0.41	0.04	0.07	0.64	0.71	0.37	0.30	0.93	0.78	0.49	0.42
q_{A^*} [e]	0.88	0.87	0.88	0.84	-0.29	-0.34	-0.24	-0.33	-0.61	-0.61	-0.62	-0.64
q_B [e]	-1.10	-1.10	-1.11	-1.11	-0.06	-0.07	-0.18	-0.13	-	-	-	-
d_{A-B} [Å]	1.17	1.17	1.17	1.18	1.27	1.28	1.29	1.29	-	-	-	-
f [cm^{-1}]	1968.63	1985.14	1959.92	1963.94	1323.51	1331.73	1208.50	1234.77	851.63	908.51	793.41	870.07

For the most part, Rh and Ir yielded similar results for all the properties displayed in Table 1, with molecular adsorption energies being slightly higher on Ir with respect to Rh.

A notable exception is that Rh significantly underbound all three adsorbates in the 2×2 cell with respect to Rh in the 3×3 cell (see the paragraph below). Consequently, at 1/4 coverage, Ir resulted in a larger adsorption energy than Rh by 1.1 eV (40.5%), 0.5 eV (34.0%), and 1.9 eV (40.0%) for CO, O₂, and O, respectively. For the 1/9 coverage, the difference was much less pronounced, with Ir still binding the adsorbate more strongly, but by only 15.7%, 3.0%, and 10.3%. The stretch mode frequencies were largely independent of coverage for CO. However, for both O₂ and O, the 3×3 coverage gave significantly lower frequencies, in spite of the almost identical bond lengths. Frequencies in the presence of Ir were higher.

The PDOS plots and charge density difference contours displayed in Figures S1–S3 of the Supplementary Materials (SMs) shed light on the adsorption results. For CO adsorption (Figure S1), the donation–back donation mechanism often attributed to metal–CO binding [62] can also be clearly seen from the CDD contours. While the general picture was the same in all cases, a particularly clear example can be seen in Figure S1d, where the CO adsorbed on Ir is surrounded by a red region of charge deficiency which has the form of the CO HOMO orbital, while the blue rings around both C and the O atoms correspond to the CO LUMO orbital. Simultaneously, charge shifts also occur internally within Ir between different *d* orbitals. Overall, this resulted in a charge accumulation between Ir and C forming a bond while the C–O bond weakened due to charge loss. This behavior did not show appreciable variation between the two coverages or the two metals. The PDOS profiles and Bader charges, however, showed significant differences that could explain the trends we have outlined above. For CO adsorption in the 2×2 model, the Fermi level coincided with a spin-split orbital of mostly Rh *d*-character. The lifting of this spin degeneracy caused this state to be partially occupied and the deeper CO levels to shift up by about 2 eV towards the Fermi level with respect to the 3×3 slab. This was consistent with the much larger Rh Bader charge and the much smaller CO adsorption energy for the 1/4 coverage given in Table 1. The total charge transferred to the CO molecule was very close for the two coverages and the two metals.

O₂ can adsorb on metal substrates both in the side-on and end-on configurations [77,78]. Here, we placed the O₂ molecule in a perpendicular orientation at the beginning of the geometry optimization. All optimization processes terminated with O₂ in the end-on geometry. The O₂ molecule was activated on transition metal centers and substrates via transfer of electrons to one (the superoxo state) or two (the peroxo state) of its π^* orbitals from the metal *d* orbitals. This was accompanied by a lengthening of the bond length and decrease in the stretch mode frequency [79,80]. The results in Table 1 indicate that for both coverages and both metals, there was indeed a charge transfer of about 0.4–0.5 $|e|$ from the metal to O₂. Similarly to the case of CO, the metals in the 2×2 cells donated about 0.3 $|e|$ more than those in the 3×3 cells. However, the adsorbate charge was almost the same for both metals and both coverages. This means that the difference in the donated charge was transferred to the rest of the atoms on the surface rather than the adsorbate. In the gas and the superoxo phases, the O–O bond length was 1.21 Å and 1.33 Å, respectively. The calculated bond length in the O₂ adsorbate here was slightly larger than the gas phase, between 1.27 Å and 1.29 Å. The metals in the 1/9 coverage yielded slightly larger bond lengths and significantly lower frequencies. The CDD contours and PDOS profiles displayed in Figure S2 for both metals in the 1/4 coverage were similar. The hybrid orbital formed through the mixing of the O₂ π^* and the metal *d* orbital had a slight occupation, which accounted for the charge gain. In the 3×3 systems, this orbital was slightly split into above and below the Fermi level since it had a higher occupation. This may explain the higher adsorption energies. This state and the lower states were significantly spin-polarized for Ir at this coverage, with a total magnetization of 3.3 μ_B . All CDD clearly demonstrate the depletion of charge from the metal *d* state to the O₂ antibonding state.

Finally, the strongest adsorption among the three adsorbates studied here belonged to atomic O. The chemical bonds between all 3d, 4d, and 5d transition metals and atomic oxygen were studied at the CCSD(T) level by Moltved and Kepp [81]. In this study, both Rh and Ir, being late transition metals, were shown to have a mid-range affinity towards

O, with metal–O bond dissociation enthalpies of 4.25 eV and 4.69 eV for RhO and IrO, respectively. These results are consistent with our findings. In the same study, the charge transfer from the metal to the O atom was reported as around 0.5 $|e|$ for both metals. In our results, the O atom had a slightly higher charge for both metals and both coverages, which was about 0.6 $|e|$. The charge on the metal, on the other hand, was once again coverage-dependent, with the 1/4 coverage resulting in a higher positive charge. The CDD contours in Figure S3 clearly show the excess charge on the O atom. All PDOS plots indicate highly spin-polarized states, as expected [81].

Our findings regarding coverage so far highlight two important points. The first is that coverage definitely affects some adsorption properties, and is therefore important to consider in future calculations. And secondly, the marked difference in the stretching frequency may be used as a viable tool to experimentally distinguish the two coverages. In the rest of our work, we used the 2×2 cells for our calculations.

3.2. Rh and Ir Adsorbed on Impurity-Doped ZnO(0001)

In this section, we present our results on single-atom Rh and Ir on the Zn(0001) surface already decorated by Rh, Ir, Al, Cr, Cu, and Pd impurities. Figure 3 displays the two geometries tested during the investigation of the most favorable adsorption site of the Rh and Ir single atom. The substitutional doping metal was placed at the location of a Zn that had been removed from the surface (labeled X in the Figure), while the Rh or Ir atom (labeled M in the figure) was placed either directly on top of X or on an adjacent hollow site. The Rh and Ir adsorption energies for each doping metal and each location are listed in Table 2.

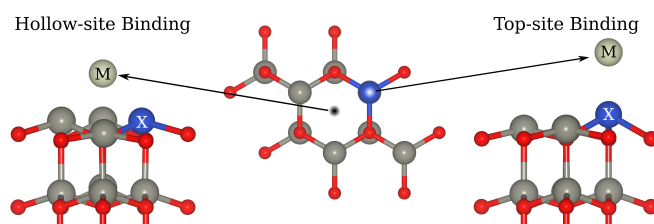


Figure 3. Top and side-view illustration of hollow and top binding geometries of single metal Ir and Rh on the impurity-enriched ZnO(0001) surface. X = Rh, Ir, Al, Cr, Cu, Pd; M = Rh, Ir. In this figure, dark gray, red, navy blue, and yellow spheres represent Zn, O, promoter metals, and Rh/Ir atoms, respectively.

Table 2. Binding energies and metal/impurity partial Bader charges for substitutional impurities in the two geometries illustrated in Figure 3. In the upper half of the table, the metal under consideration is Rh, whereas in the lower half, it is Ir. The subscript X in q_X represents the impurities.

	Top					Hollow				
M = Rh	Rh	Al	Cr	Cu	Pd	Rh	Al	Cr	Cu	Pd
E_b [eV]	−3.94	−3.58	−3.79	−1.81	−2.38	−4.28	−4.99	−4.74	−2.74	−3.34
q_X [$ e $]	0.44	2.24	1.24	0.54	0.22	0.69	2.25	1.31	0.74	0.51
q_M [$ e $]	−0.11	−0.84	−0.45	−0.12	0.03	−0.27	−0.82	−0.52	−0.23	−0.21
M = Ir	Ir	Al	Cr	Cu	Pd	Ir	Al	Cr	Cu	Pd
E_b [eV]	−4.68	−4.10	−4.67	−2.43	−3.15	−5.80	−5.88	−5.78	−3.47	−4.16
q_X [$ e $]	0.33	2.29	1.24	0.61	0.29	0.70	2.29	1.31	0.78	0.54
q_M [$ e $]	−0.09	−1.02	−0.61	−0.27	−0.07	−0.39	−0.99	−0.65	−0.39	−0.32

For both metals, the hollow sites yielded significantly larger adsorption energies. Ir bound more strongly to all impurities than Rh in both geometries. The Rh–Rh and Ir–Ir bindings are included in our results to assess the strength of the bimetallic bond, which is important for understanding the likelihood of segregation by means of forming small

clusters. Both the Rh₂ and the Ir₂ had substantially large binding energies (among the largest presented in the Table 2), indicating that clustering was indeed an important issue to consider here.

An immediately apparent result was that in contrast to the unpromoted ZnO surface, both Rh and Ir acquired a partial negative charge. This was likely to affect the charge transferred to the molecular species, thereby changing their activation towards the reaction.

Comparing different impurities (other than Rh₂ and Ir₂), both Rh and Ir bound the most strongly on Al and Cr. Consistent with the binding strength, interaction with Al and Cr also led to the highest negative charge accumulation on Ir and Rh. This illustrates the synergistic interaction between the metal oxide surface and the impurity atom, which collectively influenced the partial charges on Rh and Ir. The surface governed the charge on the impurity, which, in turn, modulated the charge on the metal atom. In the comprehensive experimental and theoretical study by Hulva et al. [62] regarding CO adsorption on iron oxide-supported transition metals with different *d* orbital populations, it was demonstrated that as the population of *d* orbitals increased, the backdonation from the metal *d* orbital to the CO 2π* orbital increased as well. This was expected to further weaken the CO bond. Therefore, since surface doping with Al and Cr resulted in the largest charge transfer to Ir and Rh, we isolated them and studied the adsorption characteristics of CO, O₂, and O on the single metals paired with these two impurities.

Before studying the adsorbed molecules, we considered the metal–metal interaction by itself. Interestingly, from the CDD contours presented in Figure S4 for the Rh–Al, Rh–Cr, Ir–Al, and Ir–Cr pairs, one observes an accumulation of charge in the region between the two metals. The PDOS profiles presented in the same figure reveal that the coupling of the Al orbitals with Rh and Ir was rather weak, forming an orbital at the Fermi level with contributions mostly from the *d* electrons of the active metal with minor contributions from Al, Zn, and O. Interaction with Cr caused a strong spin polarization of Rh and Ir.

The optimized adsorption geometries are shown in Figure 4 and the adsorption characteristics are reported in Table 3. In all the systems considered below, Rh and Ir were placed at the hollow sites. The geometry optimization for all adsorption geometries were initiated by placing the adsorbate in an orientation perpendicular to the surface on top Rh or Ir. During the optimization process, however, all adsorbates oriented themselves to varying degrees, towards the surface with the exception of O on the Rh/Cr and Ir/Cr systems, which remained in an on-top position.

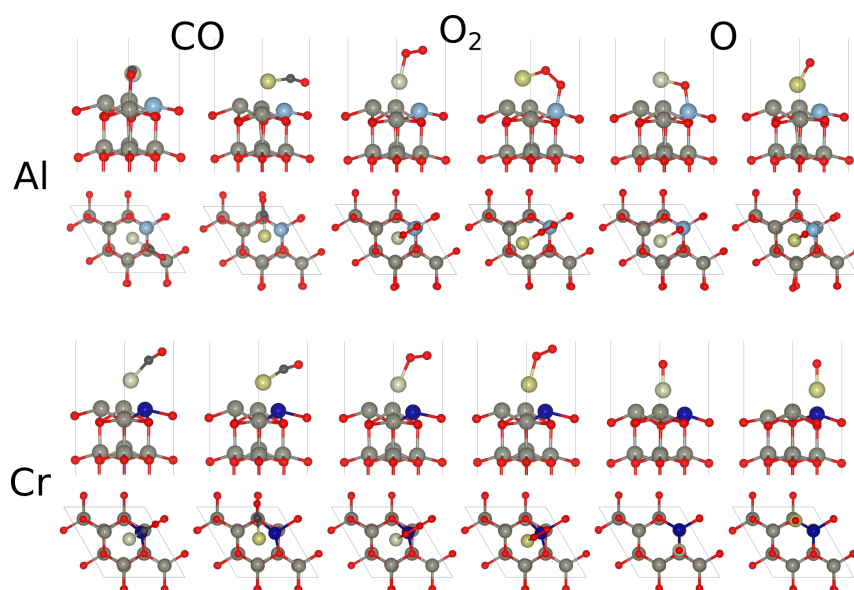


Figure 4. Optimized adsorption geometries of CO, O₂, and O on Rh and Ir placed on Al (top panels)- and Cr (bottom panels)-decorated ZnO(0001) surfaces. In this figure, blue, dark blue, dark gray, black, red, light gray, and yellow spheres represent Al, Cr, Zn, C, O, Rh, and Ir atoms, respectively.

Table 3. Adsorption energies (E_b), Bader charges (q), vibrational frequencies (f), and bond distances (d) of CO, O₂, and O on Rh and Ir placed on ZnO(0001) with substitutional Al and Cr. The subscript X stands for Rh or Ir, and Y for Al or Cr, while A and B correspond to the individual atoms of the adsorbate, respectively. The subscript (*) indicates the atom of the adsorbate directly attached to the surface. The stretch mode frequencies reported for O correspond to the O-Y bond.

	CO				O ₂				O			
	Rh-Al	Rh-Cr	Ir-Al	Ir-Cr	Rh-Al	Rh-Cr	Ir-Al	Ir-Cr	Rh-Al	Rh-Cr	Ir-Al	Ir-Cr
E_b [eV]	-2.16	-0.71	-2.50	-1.21	-0.28	-0.11	-1.91	-0.24	-5.71	-4.13	-4.24	-4.80
q_X [e]	-0.49	-0.35	-0.60	-0.37	-0.49	-0.20	0.02	-0.29	0.07	0.06	-0.28	0.05
q_Y [e]	2.30	1.32	2.34	1.35	2.26	1.31	2.42	1.30	2.43	1.26	2.31	1.27
q_{A^*} [e]	0.77	0.93	0.75	0.89	-0.19	-0.24	-0.33	-0.27	-1.12	-0.56	-0.57	-0.63
q_B [e]	-1.18	-1.08	-1.17	-1.12	-0.11	-0.12	-0.78	-0.12	-	-	-	-
d_{A-B} [Å]	1.20	1.16	1.21	1.17	1.28	1.29	1.50	1.29	-	-	-	-
f [cm ⁻¹]	1728.48	1990.71	1730.06	1940.57	1246.31	1247.60	695.95	1211.55	660.75	880.38	894.30	937.90

From the data listed in Table 3, it is immediately clear that since Al binds both Rh and Ir very strongly (see Table 2) it weakens the C–O bond. The C–O bond distance was larger than any other case reported in this work, while the vibration frequency was significantly lower. The C–O bond length and vibrational frequency were instead not much affected by the presence of Cr. For O₂, the promoting effect of the impurity was not at all evident with low adsorption energies, bond lengths close to gas phase, and large negative charges on both the noble metal and O₂. One significant exception is the O₂ adsorption geometry on the Al-Ir pair, where the molecule formed a perfect bridge between the two metals. In this case, the bond length was as large as 1.50 Å, which was consistent with the bond distance of the peroxo state, reported by Holland [79]. In this activated state, O₂ scission would occur easily. Finally, Al also yielded a higher binding energy than Cr in the case of Rh for the single O atom. However, as an exception to the trend, Cr worked somewhat better when paired with Ir. From Table 3, one notices that the stretch mode frequencies of the adsorbates show a dependence on the impurity present on the ZnO surface. In correlation with the bond length variations, Cr yielded higher frequencies with differences approaching 200 cm⁻¹. This also applies to O, while the differences (excluding the instance of dissociative adsorption) for O₂ were less pronounced.

PDOS plots for adsorption with impurities are shown in Figures 5 and 6. These profiles clearly display the difference between the mode of operation of Al and Cr as promoters. In the case of Al, the contribution was mostly indirect by means of changing the charge state of Rh. The Al contributions were very small for the electronic states near the Fermi level. In the case of Cr, due to the large number of electrons and the highly magnetic nature, the interaction was dominated by the Cr states. The systems were highly spin-polarized with a large d electron contribution from Cr near the Fermi level. The related CDD plots are given in Figure S5.

We also considered the adsorption of the CO oxidation product, CO₂, on the impurity-enriched SACs. In Figure S6 of the SM, we display the CDD contours and PDOS profiles of CO₂ adsorption on Rh and Ir on Al-decorated Zn(0001). In both cases, the geometry is one where an oxygen atom of the adsorbate binds a surface Zn atom and the C points towards Rh or Ir. The CO₂ adsorption energies are -1.54 eV and -1.60 eV for Rh and Ir, respectively. The M-C distances (M = Rh, Ir) in both cases are around 1.9 Å. The Rh and Ir partial charges are -0.49 $|e|$ and -0.61 $|e|$, respectively, while the charges on CO₂ are -0.65 $|e|$ for both metals. As expected, the negative charge state on the CO₂ molecule caused the molecule to bend. The CDD contours indicate a clear bond formation via charge accumulation in the Zn-O and M-C regions. The PDOS plots are very similar where near the Fermi energy, metal s , metal d , CO₂, and Al s states overlap.

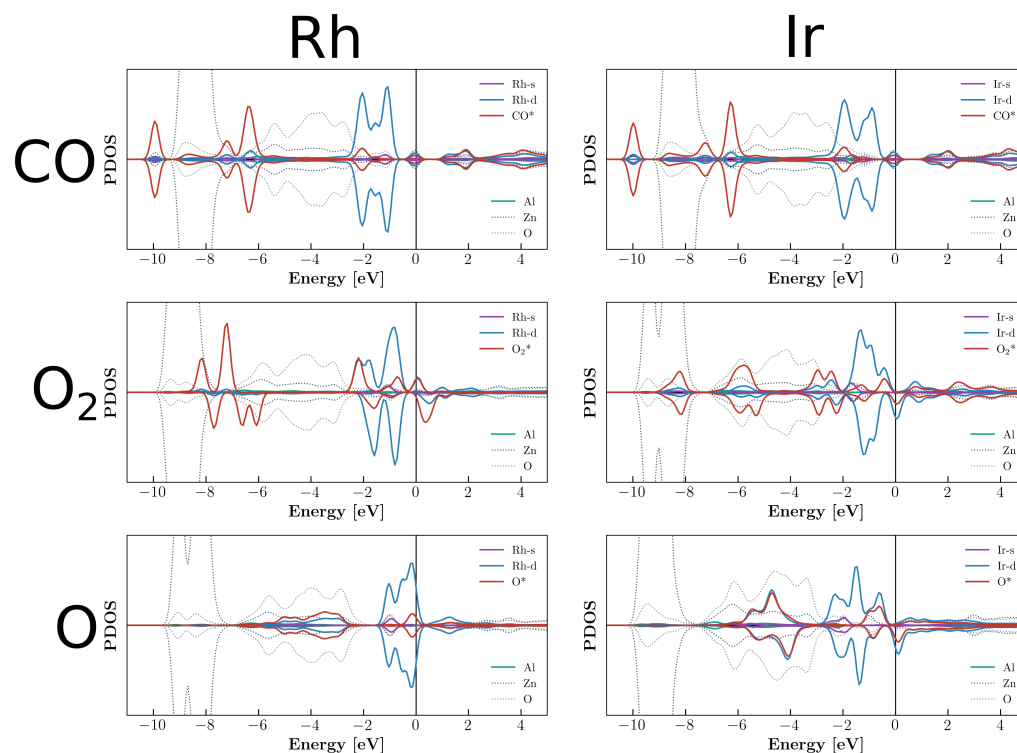


Figure 5. Partial density of states of CO, O₂, and O adsorption on Rh and Ir on the Al-decorated ZnO(0001) surface.

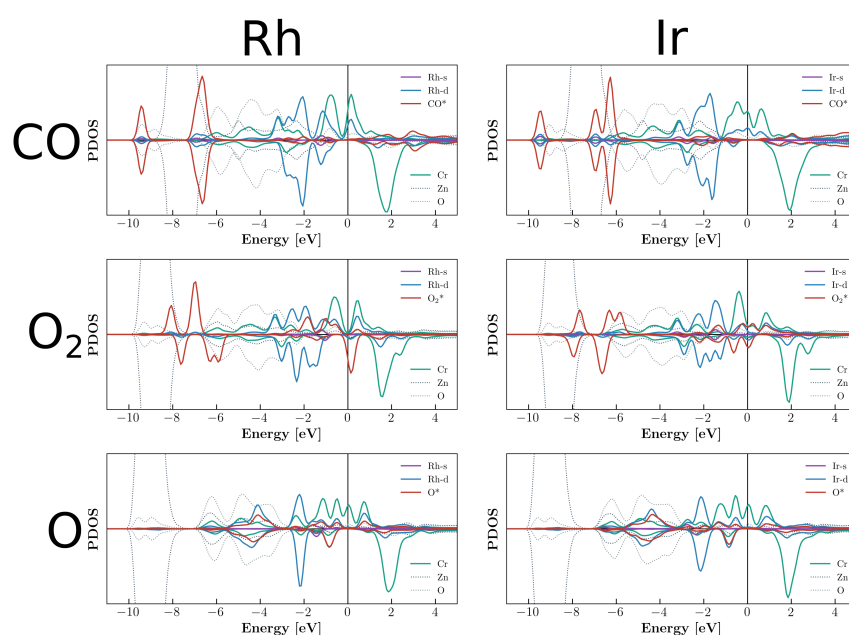


Figure 6. Partial density of states of CO, O₂, and O adsorption on Rh and Ir on the Cr-decorated ZnO(0001) surface.

4. Conclusions

In this study, we investigated the electronic structure of ZnO-supported single Rh and Ir atoms and their activity towards CO oxidation using density functional theory-based calculations and analysis tools. As indicators, we used adsorption energies, Bader partial charges, vibrational frequencies, and partial density of states analysis for the adsorption of CO, O₂, and O species. Properties of adsorption on cationic substitutional Rh and Ir atoms somewhat depended on coverage. The positive Bader charges on Rh and Ir atoms in a 2 × 2

surface cell were larger, and as a result, all adsorbates interacted less strongly. For both coverages, however, the CO bond was lengthened compared to the value in the gas-phase and the O₂ molecule was activated.

As a further step, we considered Rh and Ir single atoms on ZnO(0001) surfaces promoted by other metal atoms. Of the six screened promoters (Rh, Ir, Al, Cr, Cu, and Pd), Al and Cr yielded the largest Ir and Rh binding energies as well as Bader charges. In contrast to the Zn-substituted Rh and Ir, the Bader charges on both metals on promoted surfaces were negative. Upon CO adsorption, this extra *d*-orbital population on the metals resulted in the largest charge transfer to the molecular antibonding π^* orbital, weakening the C–O bond. Simultaneously, Al-promoted Ir was also seen to donate electronic charge to O₂ and thereby activate it. Both cationic substitutional and promoted Rh and Ir on ZnO(0001) have the potential to be active in CO oxidation. In further works, it would be interesting to study in detail how the charge state of Rh and Ir species influences their catalytic activity towards reactions of current interest.

Supplementary Materials: The following supporting information can be downloaded at <https://www.mdpi.com/article/10.3390/molecules29215082/s1>, Figure S1: Charge density difference (CDD) contours and partial density of states (PDOS) of CO adsorbed on 2 × 2 and 3 × 3 ZnO(0001) with substitutional Rh (a),(c), and Ir(b),(d). In the CDD plots red and blue regions correspond to electron deficiency and excess, respectively. Figure S2: Charge density difference (CDD) contours and partial density of states (PDOS) of O₂ adsorbed on 2 × 2 and 3 × 3 ZnO(0001) with substitutional Rh (a),(c), and Ir(b),(d). In the CDD plots red and blue regions correspond to electron deficiency and excess, respectively. Figure S3: Charge density difference (CDD) contours and partial density of states (PDOS) of O adsorbed on 2 × 2 and 3 × 3 ZnO(0001) with substitutional Rh (a),(c), and Ir(b),(d). In the CDD plots red and blue regions correspond to electron deficiency and excess, respectively. Figure S4: Charge density difference (CDD) contours and partial density of states (PDOS) of Rh and Ir adsorbed on substitutionally doped Al and Cr on the Zn(0001) surface. In the CDD plots red and blue regions correspond to electron deficiency and excess, respectively. Figure S5: Charge density difference (CDD) plots for CO, O₂, and O adsorption on Rh and Ir on the Al- and Cr-decorated ZnO(0001) surface along with PDOS profiles. In the CDD plots red and blue regions correspond to electron deficiency and excess, respectively. Figure S6: Charge density difference (CDD) plots for O₂ adsorption on Rh and Ir on the Al-decorated ZnO(0001) surface along with PDOS profiles. In the CDD plots, the blue regions indicate charge excess and the red regions charge depletion.

Author Contributions: Conceptualization, H.U. and D.T.; methodology, A.E., H.U. and D.T.; software, A.E.; validation, A.E., H.U. and D.T.; formal analysis, A.E., H.U. and D.T.; investigation, A.E., H.U. and D.T.; resources, H.U. and D.T.; data curation, A.E., H.U. and D.T.; writing—original draft preparation, H.U. and D.T.; writing—review and editing, A.E., H.U. and D.T.; visualization, A.E. and H.U.; supervision, H.U. and D.T.; project administration, H.U.; funding acquisition, H.U. and D.T. All authors have read and agreed to the published version of the manuscript.

Funding: This research was funded by the Scientific and Technological Research Council of Turkey (TÜBİTAK), Grant No: 118F355. Computational resources were provided by the National Center of Academic Network and Information (TÜBİTAK ULAKBİM) and the National Center for High Performance Computing (UHEM), Grant No. 5003342014. We furthermore acknowledge high-performance computational resources made available under the ISCRA initiative of CINECA (Italy).

Data Availability Statement: The data that support the findings of this study are available from the corresponding author upon reasonable request.

Conflicts of Interest: The authors declare no conflicts of interest.

Abbreviations

The following abbreviations are used in this manuscript:

SACs	Single-atom catalysts
DFT	Density Functional Theory
PBE	Perdew–Burke–Ernzerhof exchange correlation potential
PAW	projector-augmented-wave scheme
PDOS	Partial Density of States
CDD	Charge density difference
SM	Supplementary Material

References

1. Chen, Z.; Liu, J.; Koh, M.J.; Loh, K.P. Single-Atom Catalysis: From Simple Reactions to the Synthesis of Complex Molecules. *Adv. Mater.* **2021**, *34*, 2103882. [[CrossRef](#)] [[PubMed](#)]
2. Di Liberto, G.; Cipriano, L.A.; Pacchioni, G. Single Atom Catalysts: What Matters Most, the Active Site or The Surrounding? *ChemCatChem* **2022**, *14*, e202200611. [[CrossRef](#)]
3. Wang, A.; Li, J.; Tao, Z. Heterogeneous single-atom catalysis. *Nat. Rev. Chem.* **2018**, *2*, 65–81. [[CrossRef](#)]
4. Qiao, B.; Liu, J.; Wang, Y.; Lin, Q.; Liu, X.; Wang, A.; Li, J.; Zhang, T.; Liu, J.J. Highly Efficient Catalysis of Preferential Oxidation of CO in H₂-Rich Stream by Gold Single-Atom Catalysts. *ACS Catal.* **2015**, *5*, 6249–6254. [[CrossRef](#)]
5. Jones, J.; Xiong, H.; DeLaRiva, A.; Peterson, E.J.; Pham, H.N.; Challa, S.R.; Qi, G.; Oh, S.H.; Wiebenga, M.H.; Hernandez, X.I.P.; et al. Thermally stable single-atom platinum-on-ceria catalysts via atom trapping. *Science* **2016**, *353*, 150–154. [[CrossRef](#)] [[PubMed](#)]
6. Gawish, M.A.; Drmoseh, Q.A.; Onaizi, S.A. Single Atom Catalysts: An Overview of the Coordination and Interactions with Metallic Supports. *Chem. Rec.* **2022**, *22*, e202100328. [[CrossRef](#)]
7. Ma, F.; Chang, Q.; Yin, Q.; Sui, Z.; Zhou, X.; Chen, D.; Zhu, Y. Rational screening of single-atom-doped ZnO catalysts for propane dehydrogenation from microkinetic analysis. *Catal. Sci. Technol.* **2020**, *10*, 4938–4951. [[CrossRef](#)]
8. Han, Z.; Gao, Y. Water Adsorption and Dissociation on Ceria-Supported Single-Atom Catalysts: A First-Principles DFT+U Investigation. *Chemistry* **2016**, *22*, 2092–2099. [[CrossRef](#)] [[PubMed](#)]
9. Yang, X.; Wang, A.; Qiao, B.; Li, J.; Liu, J.J.; Zhang, T. Single-atom catalysts: A new frontier in heterogeneous catalysis. *Acc. Chem. Res.* **2013**, *46*, 1740–1748. [[CrossRef](#)]
10. Lang, R.; Du, X.; Huang, Y.; Jiang, X.; Zhang, Q.; Guo, Y.; Liu, K.; Qiao, B.; Wang, A.; Zhang, T. Single-Atom Catalysts Based on the Metal-Oxide Interaction. *Chem. Rev.* **2020**, *120*, 11986–12043. [[CrossRef](#)]
11. Li, R.; Luo, L.; Ma, X.; Wu, W.; Wang, M.; Zeng, J. Single atoms supported on metal oxides for energy catalysis. *J. Mater. Chem. A* **2021**, *10*, 5717–5742. [[CrossRef](#)]
12. Liu, J.J.; Duan, S.; Xu, J.; Qiao, B.; Lou, Y. Catalysis by Supported Single Metal Atoms. *Microsc. Microanal.* **2016**, *22*, 860–861. [[CrossRef](#)]
13. Zhou, X.; Chen, L.; Sterbinsky, G.E.; Mukherjee, D.; Unocic, R.R.; Tait, S.L. Pt-Ligand single-atom catalysts: Tuning activity by oxide support defect density. *Catal. Sci. Technol.* **2020**, *10*, 3353–3365. [[CrossRef](#)]
14. Farpón, M.G.; Henao, W.; Plessow, P.N.; Andrés, E.; Arenal, R.; Marini, C.; Agostini, G.; Studt, F.; Prieto, G. Rhodium Single-Atom Catalyst Design through Oxide Support Modulation for Selective Gas-Phase Ethylene Hydroformylation. *Angew. Chem. (Int. Ed.)* **2022**, *62*, e202214048. [[CrossRef](#)]
15. Wang, L.; Zhang, W.; Wang, S.; Gao, Z.; Luo, Z.; Wang, X.; Zeng, R.; Li, A.; Li, H.; Wang, M.; et al. Atomic-level insights in optimizing reaction paths for hydroformylation reaction over Rh/CoO single-atom catalyst. *Nat. Commun.* **2016**, *7*, 14036. [[CrossRef](#)]
16. Gu, X.K.; Qiao, B.; Huang, C.; Ding, W.; Sun, K.; Zhan, E.; Zhang, T.; Liu, J.J.; Li, W. Supported Single Pt₁/Au₁ Atoms for Methanol Steam Reforming. *ACS Catal.* **2014**, *4*, 3886–3890. [[CrossRef](#)]
17. Humayun, M.H.; Israr, M.; Li, Z.; Luo, W.; Wang, C. Metal oxides confine single atoms toward efficient thermal catalysis. *Coord. Chem. Rev.* **2023**, *488*, 215189. [[CrossRef](#)]
18. Shi, J.; Zhao, X.; Zhang, L.; Xue, X.; Guo, Z.; Guo, Z.; Gao, Y.; Gao, Y.; Li, S.F. An oxidized magnetic Au single atom on doped TiO₂(110) becomes a high performance CO oxidation catalyst due to the charge effect. *J. Mater. Chem.* **2017**, *5*, 19316–19322. [[CrossRef](#)]
19. Searles, K.; Chan, K.W.; Burak, J.A.M.; Zemlyanov, D.Y.; Safonova, O.V.; Copéret, C. Highly Productive Propane Dehydrogenation Catalyst Using Silica-Supported Ga-Pt Nanoparticles Generated from Single-Sites. *J. Am. Chem. Soc.* **2018**, *140*, 11674–11679. [[CrossRef](#)]
20. Rochlitz, L.; Searles, K.; Alfke, J.L.; Zemlyanov, D.Y.; Safonova, O.V.; Copéret, C. Silica-supported, narrowly distributed, subnanometric Pt–Zn particles from single sites with high propane dehydrogenation performance. *Chem. Sci.* **2019**, *11*, 1549–1555. [[CrossRef](#)]
21. Rochlitz, L.; Fischer, J.W.A.; Pessemesse, Q.; Clark, A.H.; Ashuiev, A.; Klose, D.; Payard, P.; Jeschke, G.; Copéret, C. Ti-Doping in Silica-Supported PtZn Propane Dehydrogenation Catalysts: From Improved Stability to the Nature of the Pt–Ti Interaction. *JACS Au* **2023**, *3*, 1939–1951. [[CrossRef](#)] [[PubMed](#)]
22. Han, B.; Lang, R.; Tang, H.; Xu, J.; Gu, X.K.; Qiao, B.; Liu, J.J. Superior activity of Rh₁/ZnO single-atom catalyst for CO oxidation. *Chin. J. Catal.* **2019**, *40*, 1847–1853. [[CrossRef](#)]

23. Butburee, T.; Prasert, A.; Rungtaweivoranit, B.; Khemthong, P.; Mano, P.; Youngjan, S.; Phanthasri, J.; Namuangruk, S.; Faungnawakij, K.; Zhang, L.; et al. Engineering Lewis-Acid Defects on ZnO Quantum Dots by Trace Transition-Metal Single Atoms for High Glycerol-to-Glycerol Carbonate Conversion. *Small* **2024**, 2403661. [[CrossRef](#)]
24. Wang, Y.F.; Qi, M.Y.; Conte, M.; Tang, Z.R.; Xu, Y.J. Bimetallic Single Atom/Nanoparticle Ensemble for Efficient Photochemical Cascade Synthesis of Ethylene from Methane. *Angew. Chem. Int. Ed.* **2024**, 63, e202407791. [[CrossRef](#)]
25. Jacobo-Fernandez, J.M.; Corona-García, C.A.; Ponce-Perez, R.; Borbon-Nunez, H.A.; Hoat, D.M.; Reyes-Serrato, A.; Guerrero-Sanchez, J. Spin-Polarized Total-Energy Calculations on Designing Magnetic Single-Atom Catalysts on the ZnO(000-1) Surface with Pt and Pd. *ACS Appl. Nano Mater.* **2023**, 6, 16740–16748. [[CrossRef](#)]
26. Mohite, S.V.; Kim, S.; Bae, J.; Jeong, H.J.; Kim, T.W.; Choi, J.; Kim, Y. Defects Healing of the ZnO Surface by Filling with Au Atom Catalysts for Efficient Photocatalytic H₂ Production. *Small* **2024**, 20, 2304393. [[CrossRef](#)]
27. Ghosh, T.K.; Nair, N.N. Rh₁/γ-Al₂O₃ Single-Atom Catalysis of O₂ Activation and CO Oxidation: Mechanism, Effects of Hydration, Oxidation State, and Cluster Size. *ChemCatChem* **2013**, 5, 1811–1821. [[CrossRef](#)]
28. Albrahim, M.; Shrotri, A.; Unocic, R.R.; Hoffman, A.S.; Bare, S.R.; Karim, A.M. Size-Dependent Dispersion of Rhodium Clusters into Isolated Single Atoms at Low Temperature and the Consequences for CO Oxidation Activity. *Angew. Chem.* **2023**, 62, e202308002. [[CrossRef](#)]
29. Song, W.; Jansen, A.P.J.; Hensen, E.J.M. A computational study of the influence of the ceria surface termination on the mechanism of CO oxidation of isolated Rh atoms. *Faraday Discuss.* **2013**, 162, 281–292. [[CrossRef](#)] [[PubMed](#)]
30. García-Vargas, C.E.; Pereira-Hernández, X.I.; Jiang, D.; Alcalá, R.; DeLaRiva, A.; Datye, A.K.; Wang, Y. Highly Active and Stable Single Atom Rh₁/CeO₂ Catalyst for CO Oxidation during Redox Cycling. *ChemCatChem* **2023**, 15, e202201210. [[CrossRef](#)]
31. Zhang, B.; Asakura, H.; Yan, N. Atomically Dispersed Rhodium on Self-Assembled Phosphotungstic Acid: Structural Features and Catalytic CO Oxidation Properties. *Ind. Eng. Chem. Res.* **2017**, 56, 3578–3587. [[CrossRef](#)]
32. Hülsey, M.J.; Zhang, B.; Ma, Z.; Asakura, H.; Do, D.; Chen, W.; Tanaka, T.; Zhang, P.; Wu, Z.; Yan, N. In situ spectroscopy-guided engineering of rhodium single-atom catalysts for CO oxidation. *Nat. Commun.* **2019**, 10, 1330. [[CrossRef](#)] [[PubMed](#)]
33. Zhang, L.L.; Sun, M.J.; Liu, C.G. CO oxidation on the phosphotungstic acid supported Rh single-atom catalysts via Rh-assisted Mars-van Krevelen mechanism. *Mol. Catal.* **2019**, 462, 37–45. [[CrossRef](#)]
34. Xu, G.; Liu, F.; Lu, Z.; Talib, S.H.; Ma, D.; Yang, Z. Design of promising single Rh atom catalyst for CO oxidation based on Graphdiyne sheets. *Phys. E-Low Syst. Nanostructures* **2021**, 130, 114676. [[CrossRef](#)]
35. Guan, H.; Lin, J.; Qiao, B.; Yang, X.; Li, L.; Miao, S.; Liu, J.J.; Wang, A.; Wang, X.; Zhang, T. Catalytically Active Rh Sub-Nanoclusters on TiO₂ for CO Oxidation at Cryogenic Temperatures. *Angew. Chem.* **2016**, 55, 2820–2824. [[CrossRef](#)]
36. Tang, Y.; Asokan, C.; Xu, M.; Graham, G.W.; Pan, X.; Christopher, P.; Li, J.; Sautet, P. Rh single atoms on TiO₂ dynamically respond to reaction conditions by adapting their site. *Nat. Commun.* **2019**, 10, 4488. [[CrossRef](#)]
37. Li, F.; Li, Y.; Zeng, X.C.; Chen, Z. Exploration of High-Performance Single-Atom Catalysts on Support M₁/FeO_x for CO Oxidation via Computational Study. *ACS Catal.* **2015**, 5, 544–552. [[CrossRef](#)]
38. Amsler, J.; Sarma, B.B.; Agostini, G.; Prieto, G.; Plessow, P.N.; Studt, F. Prospects of Heterogeneous Hydroformylation with Supported Single Atom Catalysts. *J. Am. Chem. Soc.* **2020**, 142, 5087–5096. [[CrossRef](#)]
39. Jurado, L.; Esvan, J.; Luque-Álvarez, L.A.; Bobadilla, L.F.; Odriozola, J.; Posada-Pérez, S.; Poater, A.; Comas-Vives, A.; Axet, M.R. Highly dispersed Rh single atoms over graphitic carbon nitride as a robust catalyst for the hydroformylation reaction. *Catal. Sci. Technol.* **2023**, 13, 1425–1436. [[CrossRef](#)]
40. Wang, C.; Gu, X.K.; Yan, H.; Lin, Y.; Li, J.; Liu, D.; Li, W.; Lu, J. Water-Mediated Mars–Van Krevelen Mechanism for CO Oxidation on Ceria-Supported Single-Atom Pt₁ Catalyst. *ACS Catal.* **2017**, 7, 887–891. [[CrossRef](#)]
41. Lang, R.; Li, T.; Matsumura, D.; Miao, S.; Ren, Y.; Cui, Y.; Tan, Y.; Qiao, B.; Li, L.; Wang, A.; et al. Hydroformylation of Olefins by a Rhodium Single-Atom Catalyst with Activity Comparable to RhCl(PPh₃)₃. *Angew. Chem.* **2016**, 55, 16054–16058. [[CrossRef](#)] [[PubMed](#)]
42. Hu, Y.; Chen, C.; Shen, T.; Guo, X.; Yang, C.; Wang, D.; Zhu, Y. Hollow Carbon Nanorod Confined Single Atom Rh for Direct Formic Acid Electrooxidation. *Adv. Sci.* **2022**, 9, 2205299. [[CrossRef](#)] [[PubMed](#)]
43. Matsubu, J.C.; Yang, V.N.; Christopher, P. Isolated metal active site concentration and stability control catalytic CO₂ reduction selectivity. *J. Am. Chem. Soc.* **2015**, 137, 3076–3084. [[CrossRef](#)]
44. Lin, J.; Wang, A.; Qiao, B.; Liu, X.; Yang, X.; Wang, X.; Liang, J.; Li, J.; Liu, J.J.; Tao, Z. Remarkable performance of Ir₁/FeO_x single-atom catalyst in water gas shift reaction. *J. Am. Chem. Soc.* **2013**, 135, 15314–15317. [[CrossRef](#)]
45. Liang, J.X.; Lin, J.; Yang, X.; Wang, A.; Qiao, B.; Liu, J.J.; Zhang, T.; Li, J. Theoretical and Experimental Investigations on Single-Atom Catalysis: Ir₁/FeO_x for CO Oxidation. *J. Phys. Chem. C* **2014**, 118, 21945–21951. [[CrossRef](#)]
46. Lu, Y.; Wang, J.; Yu, L.; Kovarik, L.; Zhang, X.; Hoffman, A.S.; Gallo, A.; Bare, S.R.; Sokaras, D.; Kroll, T.; et al. Identification of the active complex for CO oxidation over single-atom Ir-on-MgAl₂O₄ catalysts. *Nat. Catal.* **2018**, 2, 149–156. [[CrossRef](#)]
47. Liang, J.X.; Lin, J.; Liu, J.J.; Wang, X.; Zhang, T.; Li, J. Dual metal active sites in an Ir₁/FeO_x single-atom catalyst: A redox mechanism for the water-gas-shift reaction. *Angew. Chem.* **2020**, 59, 12868. [[CrossRef](#)]
48. Akça, A.; Karaman, O.; Karaman, C.; Atar, N.; Yola, M.L. A comparative study of CO catalytic oxidation on the single vacancy and di-vacancy graphene supported single-atom iridium catalysts: A DFT analysis. *Surf. Interfaces* **2021**, 25, 101293. [[CrossRef](#)]

49. Chen, L.; Ali, I.S.; Sterbinsky, G.E.; Zhou, X.; Wasim, E.; Tait, S.L. Ligand-coordinated Ir single-atom catalysts stabilized on oxide supports for ethylene hydrogenation and their evolution under a reductive atmosphere. *Catal. Sci. Technol.* **2021**, *11*, 2081–2093. [[CrossRef](#)]
50. Lin, S.; Ye, X.; Johnson, R.S.; Guo, H. First-Principles Investigations of Metal (Cu, Ag, Au, Pt, Rh, Pd, Fe, Co, and Ir) Doped Hexagonal Boron Nitride Nanosheets: Stability and Catalysis of CO Oxidation. *J. Phys. Chem. C* **2013**, *117*, 17319–17326. [[CrossRef](#)]
51. Chen, M.; Serna, P.; Lu, J.; Gates, B.C.; Dixon, D.A. Molecular models of site-isolated cobalt, rhodium, and iridium catalysts supported on zeolites: Ligand bond dissociation energies. *Comput. Theor. Chem.* **2015**, *1074*, 58–72. [[CrossRef](#)]
52. Karmakar, S.; Chowdhury, C.; Datta, A. Noble-Metal-Supported GeS Monolayer as Promising Single-Atom Catalyst for CO Oxidation. *J. Phys. Chem. C* **2018**, *122*, 14488–14498. [[CrossRef](#)]
53. Tan, K.; Dixit, M.; Dean, J.; Mpourmpakis, G. Predicting Metal-Support Interactions in Oxide-Supported Single-Atom Catalysts. *Ind. Eng. Chem. Res.* **2019**, *58*, 20236–20246. [[CrossRef](#)]
54. Sarma, B.B.; Plessow, P.N.; Agostini, G.; Concepción, P.; Pfänder, N.; Kang, L.; Wang, F.R.; Studt, F.; Prieto, G. Metal-specific reactivity in single-atom-catalysts: CO oxidation on 4d and 5d transition metals atomically dispersed on MgO. *J. Am. Chem. Soc.* **2020**, *142*, 14890–14902. [[CrossRef](#)] [[PubMed](#)]
55. Liu, C.G.; Zhang, L.L.; Chen, X.M. CO oxidation over the polyoxometalate-supported single-atom catalysts M_1/POM (Fe, Co, Mn, Ru, Rh, Os, Ir, and Pt; $POM = [PW_{12}O_{40}]^{3-}$): A computational study on the activation of surface oxygen species. *Dalton Trans.* **2019**, *48*, 6228–6235. [[CrossRef](#)]
56. Qi, R.; Zhu, B.; Han, Z.; Gao, Y. High-Throughput Screening of Stable Single-Atom Catalysts in CO₂ Reduction Reactions. *ACS Catal.* **2022**, *12*, 8269–8278. [[CrossRef](#)]
57. Wang, R.; Zheng, J.C. ZnO monolayer-supported single atom catalysts for efficient electrocatalytic hydrogen evolution reaction. *Phys. Chem. Chem. Phys.* **2024**, *26*, 5848–5857. [[CrossRef](#)]
58. Xie, X.; Li, Y.; Liu, Z.; Haruta, M.M.; Shen, W. Low-temperature oxidation of CO catalysed by Co₃O₄ nanorods. *Nature* **2009**, *458*, 746–749. [[CrossRef](#)]
59. Freund, H.; Meijer, G.; Scheffler, M.; Schlögl, R.; Wolf, M. CO oxidation as a prototypical reaction for heterogeneous processes. *Angew. Chem.* **2011**, *50*, 10064–10094. [[CrossRef](#)]
60. Falsig, H.; Hvolbaek, B.; Kristensen, I.S.; Jiang, T.; Bligaard, T.; Christensen, C.H.; Nørskov, J.K. Trends in the catalytic CO oxidation activity of nanoparticles. *Angew. Chem.* **2008**, *47*, 4835–4839. [[CrossRef](#)]
61. Liang, J.X.; Yu, Q.; Yang, X.; Zhang, T.; Li, J. A systematic theoretical study on FeO_x-supported single-atom catalysts: M_1/FeO_x for CO oxidation. *Nano Res.* **2018**, *11*, 1599–1611. [[CrossRef](#)]
62. Hulva, J.; Meier, M.; Bliem, R.; Jakub, Z.; Kraushofer, F.; Schmid, M.; Diebold, U.; Franchini, C.; Parkinson, G.S. Unraveling CO adsorption on model single-atom catalysts. *Science* **2021**, *371*, 375–379. [[CrossRef](#)] [[PubMed](#)]
63. Jin, H.; Zhou, K.; Zhang, R.; Cui, H.; Yu, Y.; Cui, P.; Song, W.; Cao, C. Regulating the electronic structure through charge redistribution in dense single-atom catalysts for enhanced alkene epoxidation. *Nat. Commun.* **2023**, *14*, 2494. [[CrossRef](#)]
64. Meunier, F.C. Relevance of IR Spectroscopy of Adsorbed CO for the Characterization of Heterogeneous Catalysts Containing Isolated Atoms. *J. Phys. Chem. C* **2021**, *125*, 21810–21823. [[CrossRef](#)]
65. Kresse, G.; Hafner, J. Ab initio molecular dynamics for liquid metals. *Phys. Rev. B* **1993**, *47*, 558–561. [[CrossRef](#)]
66. Kresse, G.; Furthmüller, J. Efficiency of ab-initio total energy calculations for metals and semiconductors using a plane-wave basis set. *Comput. Mater. Sci.* **1996**, *6*, 15–50. [[CrossRef](#)]
67. Kresse, G.; Furthmüller, J. Efficient iterative schemes for ab initio total-energy calculations using a plane-wave basis set. *Phys. Rev. B* **1996**, *54*, 11169–11186. [[CrossRef](#)]
68. Perdew, J.P.; Burke, K.; Ernzerhof, M. Generalized Gradient Approximation Made Simple. *Phys. Rev. Lett.* **1996**, *77*, 3865–3868. [[CrossRef](#)]
69. Blöchl, P.E. Projector augmented-wave method. *Phys. Rev. B* **1994**, *50*, 17953–17979. [[CrossRef](#)]
70. Kresse, G.; Joubert, D. From ultrasoft pseudopotentials to the projector augmented-wave method. *Phys. Rev. B* **1999**, *59*, 1758–1775. [[CrossRef](#)]
71. Dudarev, S.L.; Botton, G.A.; Savrasov, S.Y.; Humphreys, C.J.; Sutton, A.P. Electron-energy-loss spectra and the structural stability of nickel oxide: An LSDA+U study. *Phys. Rev. B* **1998**, *57*, 1505–1509. [[CrossRef](#)]
72. Harun, K.; Salleh, N.A.; Deghfel, B.; Yaakob, M.K.; Mohamad, A.A. DFT + U calculations for electronic, structural, and optical properties of ZnO wurtzite structure: A review. *Results Phys.* **2020**, *16*, 102829. [[CrossRef](#)]
73. Meyer, B.; Marx, D. Density-functional study of the structure and stability of ZnO surfaces. *Phys. Rev. B* **2003**, *67*, 035403. [[CrossRef](#)]
74. Tang, W.; Sanville, E.; Henkelman, G. A grid-based Bader analysis algorithm without lattice bias. *J. Phys. Condens. Matter* **2009**, *21*, 084204. [[CrossRef](#)]
75. Xue, Z.; Gao, X.; Zhang, Y.; Yan, M.; Xu, J.; Wu, Y. Site-coverage dependent single-atom-layer catalysts toward hydrogen production. *Chem Catal.* **2023**, *3*, 100538. [[CrossRef](#)]
76. Lausche, A.C.; Medford, A.J.; Khan, T.S.; Xu, Y.; Bligaard, T.; Abild-Pedersen, F.; Nørskov, J.K.; Studt, F. On the effect of coverage-dependent adsorbate–adsorbate interactions for CO methanation on transition metal surfaces. *J. Catal.* **2013**, *307*, 275–282. [[CrossRef](#)]

77. Silva, J.C.M.; dos Santos, E.C.; Heine, T.; De Abreu, H.A.; Duarte, H.A. Oxidation Mechanism of Arsenopyrite in the Presence of Water. *J. Phys. Chem. C* **2017**, *121*, 26887–26894. [[CrossRef](#)]
78. Gao, Z.y.; Yang, W.j.; Ding, X.l.; Lv, G.; Yan, W.p. Support effects on adsorption and catalytic activation of O₂ in single atom iron catalysts with graphene-based substrates. *Phys. Chem. Chem. Phys.* **2018**, *20*, 7333–7341. [[CrossRef](#)]
79. Holland, P.L. Metal–dioxygen and metal–dinitrogen complexes: Where are the electrons? *Dalton Trans.* **2010**, *39*, 5415–5425. [[CrossRef](#)]
80. Hess, F.; Staykov, A.T.; Yildiz, B.; Kilner, J., Solid Oxide Fuel Cell Materials and Interfaces. In *Handbook of Materials Modeling: Applications: Current and Emerging Materials*; Springer International Publishing: Cham, Switzerland, 2018; pp. 1–31.
81. Moltved, K.A.; Kepp, K.P. The Chemical Bond between Transition Metals and Oxygen: Electronegativity, d-Orbital Effects, and Oxophilicity as Descriptors of Metal–Oxygen Interactions. *J. Phys. Chem. C* **2019**, *123*, 18432–18444. [[CrossRef](#)]

Disclaimer/Publisher’s Note: The statements, opinions and data contained in all publications are solely those of the individual author(s) and contributor(s) and not of MDPI and/or the editor(s). MDPI and/or the editor(s) disclaim responsibility for any injury to people or property resulting from any ideas, methods, instructions or products referred to in the content.